International Journal of Non–Linear Mechanics 166 (2024) 104858

Contents lists available at ScienceDirect

International Journal of Non-Linear Mechanics

journal homepage: www.elsevier.com/locate/nlm

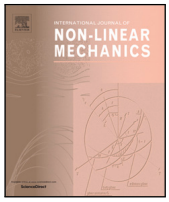

Periodic response and stability analysis of a bistable viscoelastic von Mises truss

Pritam Ghoshal [a,b], James M. Gibert [a,b,*], Anil K. Bajaj [b]

[a] Advanced Dynamics and Mechanics Lab, USA
[b] Ray W. Herrick Laboratories, School of Mechanical Engineering, Purdue University, West Lafayette, IN 47907, USA

ARTICLE INFO

Keywords:
Bifurcation
Bistability
Harmonic balance
Viscoelasticity
Viscosity
von Mises truss

ABSTRACT

This paper examines the effect of viscoelasticity on the periodic response of a lumped parameter viscoelastic von Mises truss. The viscoelastic system is described by a second-order equation that governs the mechanical motion coupled to a first-order equation that governs the time evolution of the viscoelastic forces. The viscoelastic force evolves at a much slower rate than the elastic oscillations in the system. This adds additional time scales and degrees of freedom to the system compared to its viscous counterparts. The focus of this study is on the system's behavior under harmonic loading, which is expected to show both regular and chaotic dynamics for certain combinations of forcing frequency and amplitude. While the presence of chaos in this system has already been demonstrated, we shall concentrate only on the periodic solutions. The presence of the intrawell and interwell periodic oscillations is revealed using the Harmonic Balance method. The study also looks at the influence of parameter changes on the system's behavior through bifurcation diagrams, which enable us to identify optimal system parameters for maximum energy dissipation. Lastly, we formulate an equivalent viscous system using an energy-based approach. We observe that a naive viscous model fails to capture the behavior accurately depending on the system and excitation parameters, as well as the type of excitation. This underscores the necessity to study the full-scale viscoelastic system.

1. Introduction

The study of multistable systems has been an area of active research for the past few decades [1]. The interest in these types of systems stems from their inherent capability to exist in multiple states without requiring a constant application of an external force. These systems have been exploited for applications ranging from motion of robotic systems, programmable material, energy absorption, to energy harvesting [2]. In this paper, we focus on bistable systems, i.e. systems with two stable states. Specifically, we will examine the dynamics of a harmonically excited, bistable viscoelastic truss with two states: a natural state and an inverted state.

This representation as a truss is of particular interest to the engineering community, as it captures the dynamics of bistable viscoelastic dome-shaped structures and bistable arches [3,4]. Typically, these systems have been studied either experimentally or through finite element simulations because they give a more concrete picture of the system's dynamics. Besides having nonlinear deflections, the existence of multiple equilibria, these caps/domes also exhibit pseudo-bistability ('temporary bistability' that involves a slow creeping motion followed by a rapid snap-through [5–10] due to a slowly changing stiffness when the structure is held just beyond a snap-through threshold and released) have been studied previously in [11–13]. These behaviors have inspired many studies. Montalvo et al. [14] studied the effect of geometry on the periodic buckling patterns of elastic shells. Taffetani et al. [15] determined the threshold between bistability and monostability of shells with different solid angles. Sobota and Seffen [16] studied the effects of boundary conditions on the stability of axisymmetric shells. They showed that restrictions to boundary movements in the plane enhance bistability, while restrictions to the rotation decrease bistability. Seffen and Vidoli [17] showed that non-axisymmetric inversion of shells is inevitable in the presence of very small initial imperfections. Brinkmeyer et al. [18] showed the effects of material and geometric parameters on the pseudo-bistability of a viscoelastic spherical dome. Despite vast research on shell theory, a full-scale analytical treatment of these systems becomes complicated. As a result, researchers tend to use various low-dimensional, usually single-degree-of-freedom models that are representative of this complex system.

In contrast to a continuous model, a lumped-parameter single degree-of-freedom system can be used to approximate the dynamics of the dome. The simplest model analogous to these dome-shaped

* Corresponding author at: Ray W. Herrick Laboratories, School of Mechanical Engineering, Purdue University, West Lafayette, IN 47907, USA.
E-mail address: jgibert@purdue.edu (J.M. Gibert).

https://doi.org/10.1016/j.ijnonlinmec.2024.104858
Received 22 January 2024; Received in revised form 1 July 2024; Accepted 25 July 2024
Available online 30 July 2024

structures is a von Mises truss, capable of exhibiting bistable behavior. The influence of boundary conditions on the bistability of the truss was studied in [19]. Gomez et al. [3] use both lumped parameter and continuous models to investigate snap-through in the presence of viscoelasticity. The lumped parameter analysis was used as a foundation for analyzing the continuous model and to obtain analytical expression for the occurrence of snap-through in time. Instabilities in viscoelastic structures have been studied in [20]. The interaction between nonlinearities and viscoelasticity was studied in [21].

While the autonomous behavior of the viscoelastic von Mises truss has garnered much interest, the dynamics of the system becomes significantly more complicated when subjected to harmonic excitation. A brief account of viscoelasticity and harmonic excitation can be found in [22]. In this case, depending on the forcing amplitude or the forcing frequency, there may be escapes from a potential well or even chaotic motions [23]. Loukaides [24] studied the transition shapes of a bistable spherical cap subjected to magnetic actuation. Suire and Cederbaum [25,26] studied the dynamics of viscoelastic bars subjected to harmonic forcing using numerical techniques and demonstrated the presence of chaos. Pourtakdoust and Fazelzadeh [27] studied viscoelastic panel flutter in a supersonic flow. [28] gives a complete review of viscoelastic materials, its characterization and response under different loading.

Perturbation methods, including harmonic balance and the method of multiple scales, have been instrumental in studying these nonlinear systems. Leadenham and Erturk [29] used a multi-term harmonic balance to investigate the enhancement of bandwidth for energy harvesting in a 'M-shaped' asymmetric non-linear oscillator. Alhussein and Daqaq [30] used the harmonic balance and multiple scales method to estimate the galloping speed and escape speed for a twin-well oscillator. Jiang et al. [31] used the harmonic balance method to study the dynamics of a Helmholtz-Duffing oscillator coupled to a nonlinear capacitance and the influence of asymmetry in potential wells. A comprehensive review of the harmonic balance method, including shooting algorithms and numerical continuation methods for various nonlinear problems, can be found in [32].

This work focuses on the effect of viscoelasticity on the periodic response of a harmonically forced von Mises truss. Viscoelasticity in autonomous systems introduces an additional degree of freedom that affects the stability of the system [33]. This gives rise to the possibility of several interesting dynamical behaviors. The viscous damper in [23] is replaced by a viscoelastic element, thereby leading to further complexity in the system, due to the additional degree of freedom. Although chaotic solutions and their boundaries have been studied in a previous work [23], this is not simply a trivial extension. Multistable systems such as these can have multiple coexisting motions. This leads to design challenges, especially if one tries to realize the large-amplitude periodic solutions alone. Hence, it is imperative to do a full-scale parametric study. We quantify the effect of parameter variations through numerical and analytical techniques. This enables us to identify the optimal system parameters for maximum energy dissipation. Finally, we propose an equivalent viscous model using an energy-based approach. We demonstrate how this simplistic model fails under certain scenarios, thus necessitating a study of the complete viscoelastic system.

2. Viscoelastic model

The undeformed configuration of the system under consideration is shown in Fig. 1(a). At this instant, both tilted springs are unstretched. The tilted springs have a stiffness of k and are inclined at an angle α_0 to the horizontal in the undeformed configuration. The width of the truss is $2w_0$. A viscoelastic standard linear solid element is attached to the mass. It consists of a damper with viscosity c and two springs, one in parallel and the other in series with the damper, of stiffness k_1 and k_2 respectively. The mass is acted on by a harmonic force $f_0 \cos \omega t$.

2.1. Model description

Let the mass be indented downward by an amount x. Assuming the small-angle approximations, the change in length of the tilted springs and the instantaneous angle made by the tilted springs with the horizontal are given as

$$dl \approx \frac{x^2 - 2w_0\alpha_0 x}{2w_0}, \qquad \alpha \approx \frac{1}{w_0}(\alpha_0 w_0 - x). \tag{1}$$

Thus the governing equation for the mass is given as [3]

$$m\frac{d^2x}{dt^2} = \frac{kx}{w_0^2}(x - 2\alpha_0 w_0)(\alpha_0 w_0 - x) - f_v + f_0 \cos \omega t, \tag{2}$$

where f_v is the force induced in the viscoelastic element. The constitutive relation for the viscoelastic unit is given as [34]

$$\frac{k_1 + k_2}{k_2}\frac{dx}{dt} + \frac{k_1}{c}x = \frac{1}{k_2}\frac{df_v}{dt} + \frac{1}{c}f_v. \tag{3}$$

2.2. Non-dimensionalization

For the viscoelastic system, there exist two time scales, one is the slow time scale of stress relaxation of $\mathcal{O}(c/k_2)$, and the other is the faster time scale of elastic oscillations of $\mathcal{O}(\alpha_0^{-1}\sqrt{m/k})$. We first rescale time with respect to the slow time. Thus, we have $t = \frac{c}{k_2}T$. The displacements are scaled with respect to the initial height of the truss in the undeformed configuration. Thus, we have $x = \alpha_0 w_0 X$. In addition, we introduce the following non-dimensional parameters into the problem.

$$D_e = \alpha_0 \frac{c/k_2}{\sqrt{m/k}}, \qquad \beta = \frac{k_2}{k_1 + k_2}, \qquad \lambda = \frac{k_1}{k\alpha_0^2}. \tag{4}$$

Here D_e is the Deborah number, which is the ratio of the timescale of stress relaxation to the timescale of elastic oscillations. β is called the relaxation parameter and is the ratio of stiffnesses in the viscoelastic unit. It controls the viscoelastic behavior of the material and ranges from zero to one ($\beta = 0$ corresponding to the elastic material). λ is a geometric/relative stiffness parameter. λ also acts as a static bifurcation parameter and governs the monostability/bistability of the truss. More details on these nondimensional parameters can be found in [3,20]. Additionally, we have

$$F_0 = \frac{f_0}{k\alpha_0^3 w_0}, \qquad \Sigma = \frac{f_v}{k_1\alpha_0 w_0}, \qquad \Omega = \omega\frac{c}{k_2}. \tag{5}$$

The governing equations are given by

$$D_e^{-2}\frac{d^2X}{dT^2} = X(X-2)(1-X) - \lambda\Sigma + F_0 \cos \Omega T, \tag{6}$$

and

$$\frac{1}{1-\beta}\frac{dX}{dT} + X = \frac{d\Sigma}{dT} + \Sigma. \tag{7}$$

3. Dynamic response

The total energy of the autonomous system (unforced and elastic) is given by

$$\Pi = \frac{1}{2}D_e^{-2}\dot{X}^2 + X^2 + \lambda\frac{X^2}{2} - X^3 + \frac{X^4}{4}, \tag{8}$$

and is shown in Fig. 1(b) for $D_e = 1$. It is immediately evident that for a given velocity $\dot{X}$ and $\lambda \neq 0$, the system will have an asymmetric potential well about the unstable saddle point. The figure also shows the trajectories corresponding to different system parameters. It is evident that while viscosity only affects the rate of decay of trajectories, viscoelasticity affects both the energy landscape (due to the elastic component) as well as the decay rate (due to the viscous component) [23]. The potential energy of the system [33] can be written as

$$V = X^2 + \lambda\frac{X^2}{2} - X^3 + \frac{X^4}{4}. \tag{9}$$

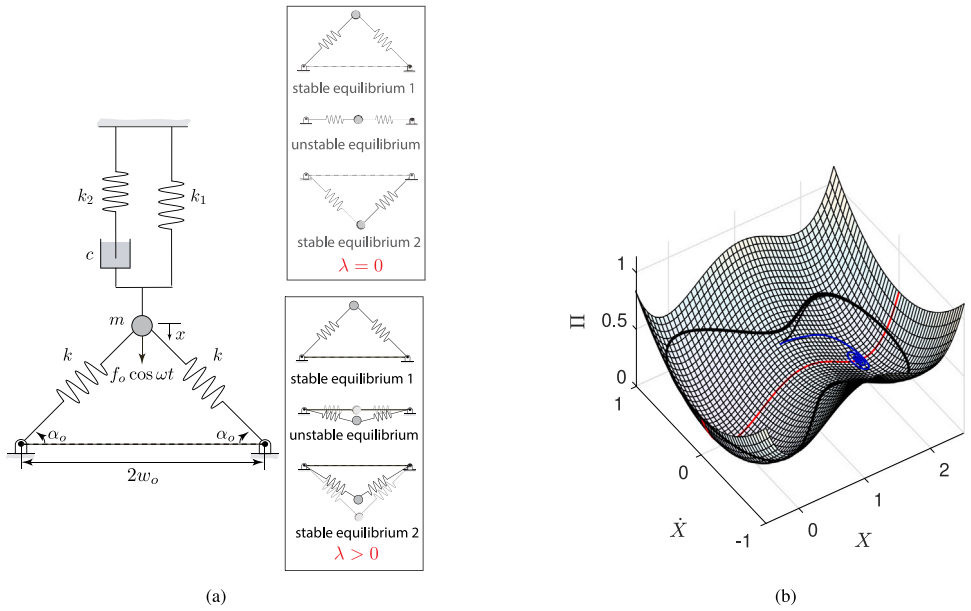

Fig. 1. Schematic and energy in the system: (a) von Mises truss with viscoelastic element subjected to harmonic forcing. Inset shows the stable and unstable equilibrium configuration for $\lambda = 0$ and $\lambda \neq 0$ (where λ is defined in Eq. (4)) (b) Total energy surface for the autonomous system for $\lambda = 0.1$. The red line represents a total energy curve for a given velocity $\dot{X}$, which is asymmetric about the saddle point. The black line represents a high-amplitude trajectory with $\beta = 0$. The blue line represents a decaying trajectory with $\beta = 0.1$. [23]. (For interpretation of the references to color in this figure legend, the reader is referred to the web version of this article.)

The equilibrium positions must satisfy $\frac{dV}{dX} = 0$ and can be written as

$$X = 0, \quad X = \frac{3 \pm \sqrt{1 - 4\lambda}}{2}. \tag{10}$$

Here $X = 0$ corresponds to the natural equilibrium configuration (which is always stable). The roots with the $\pm$ sign indicate the inverted stable configuration and the unstable configuration respectively as shown in Fig. 1(a). As noted by Gomez et al. [3] the presence of the equilibrium depends on λ. Note that λ is a static bifurcation parameter which dictates whether the truss is bistable or monostable. A shallow truss (low value of α_0 or high λ) will be monostable. On the other hand, a deeper truss (higher value of α_0 or lower λ) will be bistable. Specifically, the following can be noted:

1. When $\lambda = 0$, the system is bistable and the potential function is symmetric and has two potential wells separated by a potential barrier.
2. When $0 < \lambda \leq \frac{1}{4}$, the system is bistable; however, the potential function is asymmetric with two potential wells separated by a potential barrier. In this configuration the inverted state becomes the higher energy state.
3. When $\lambda > \frac{1}{4}$, the system is monostable with a potential having a single potential well. Additionally, the nonlinear restoring force increases monotonically from the initial equilibrium position.

We consider that the truss is initially indented by applying an instantaneous displacement of X_{ind} and held in that particular position for a duration T_{ind}, thus allowing for stress relaxation to occur. The indentation force is then removed and immediately replaced by a harmonic force, and our external clock is started, i.e., we define $T = 0$ at the time the indenter is released, and the harmonic loading is applied. To quantify the behavior of the truss during the indentation period, that is for $T < 0$, we approximate the indentation as

$$X = X_{ind} \mathrm{H}(T + T_{ind}) \tag{11}$$

where H(.) is the Heaviside function. Substituting this into the constitutive relation for the viscoelastic element, and solving for the nondimensional force Σ (noting that the derivative of the Heaviside function is the Dirac-Delta function), we obtain the initial conditions at $T = 0$ as

$$X(0^+) = X_{\text{ind}}, \quad \dot{X}(0^+) = 0, \quad \Sigma(0^+) = X_{\text{ind}} \left[1 + \frac{\beta}{1-\beta} e^{-T_{\text{ind}}}\right]. \tag{12}$$

In this paper, we take $\lambda = 0.1$, $\beta = 0.5$, $D_e = 10$, $X_{\text{ind}} = 1.5$ and $T_{\text{ind}} = 5$, unless otherwise specified. The choice of these parameters is based on experimental observations. This study was inspired by dome-shaped structures made from rubbery polymers such as silicon-based elastomers. For these systems, stress relaxation occurs on a much slower time scale than elastic oscillations [18,20,35]. Hence D_e has to be at least $O(1)$. Now, since the Deborah number governs the slow dynamics, a very high value would make it computationally intensive to resolve the fast elastic oscillations when solving for motion on the slower timescale. Hence, we choose D_e as 10. Second, λ has been chosen as 0.1 so that our system lies in the bistable zone. Fig. 2 shows the steady-state time domain response for $F_0 = 0.5$ and $F_0 = 0.8$ corresponding to periodic and chaotic oscillations. More details can be found in [23].

Since the system has a double potential well, it is very likely that, for some combination of forcing amplitude and forcing frequency, the system escapes from a potential well, exhibiting either intrawell or cross-well motion. This can be better visualized through some time-domain simulations. We start with an initial condition of $X_{\text{ind}} = 1.5$ in the right potential well. We consider a forcing frequency of $\Omega = 10$. Fig. 3(a) shows the time response for $F_0 = 0.01$. In this case, the system remains confined to the right potential well (centered around $X = 1.8873$). Fig. 3(b) shows the time response for $F_0 = 0.1$. In this case, the system initially shows large amplitude transients where it traverses both wells before finally settling into the left potential well (centered about the stable natural configuration). This indicates that the system has escaped from the potential well it started from, but it still exhibits small-amplitude intrawell motion. Fig. 3(c) shows the time response for $F_0 = 0.5$. In this case, the system keeps on transitioning from one potential well to the other and signifies large-amplitude interwell motion.

Although the system is capable of exhibiting large-amplitude chaotic motion [23], large-amplitude periodic motions are of particular interest, especially in the context of energy harvesting or vibration suppression. In the next section, we aim to find the parameter regimes in which these large-amplitude solutions may be obtained through the Harmonic Balance Method.

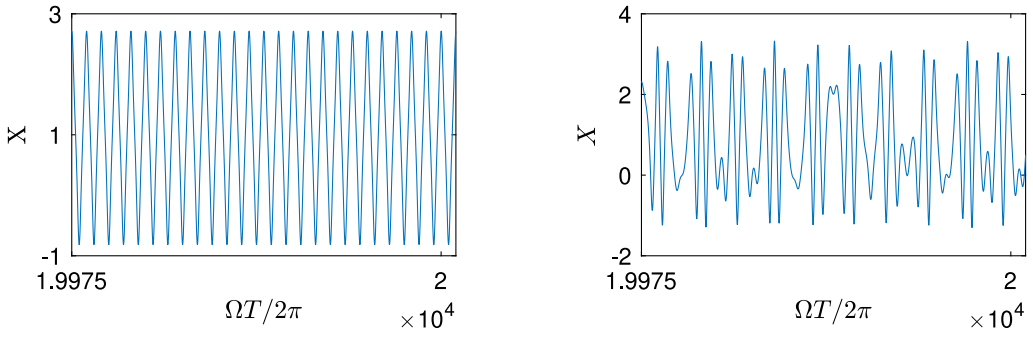

(a) $F_0 = 0.5$ (b) $F_0 = 0.8$

Fig. 2. Steady state time response for $\Omega = 10, D_e = 10, \lambda = 0.1, \beta = 0.5$ (a) Large amplitude periodic motion (b) Large amplitude chaotic motion.

4. Harmonic balance method

In this section, we aim to study the parameter space of forcing frequency and forcing amplitude where either large-amplitude cross-well oscillations or small-amplitude intra-well oscillations take place. Previous studies of similar systems have shown that the response consists of a dominant frequency equal to the frequency of excitation [36–38]. However, because of the presence of quadratic and cubic nonlinearities we note that for some combinations of forcing parameters, the subharmonic or superharmonic responses are excited. In such cases, a higher-order truncation of the Fourier series is needed.

4.1. 1-term approximation

Here we start with the single-term approximation by considering the dominant response at the excitation frequency. Thus we have,

$$X(T) = A(T) + B(T)\cos\Omega T + C(T)\sin\Omega T, \tag{13}$$

and

$$\Sigma(T) = Q(T) + M(T)\cos\Omega T + N(T)\sin\Omega T, \tag{14}$$

where the terms $A(T)$ and $Q(T)$ are needed for intra-well and inter-well oscillations with nonzero displacement bias. Here, the coefficients are functions of the slow time T. The corresponding derivatives are given as

$$\dot{X} = \dot{A} + (\dot{B} + C\Omega)\cos\Omega T + (\dot{C} - B\Omega)\sin\Omega T, \tag{15}$$

$$\dot{\Sigma} = \dot{Q} + (\dot{M} + N\Omega)\cos\Omega T + (\dot{N} - M\Omega)\sin\Omega T, \tag{16}$$

$$\ddot{X} = (2\dot{C}\Omega - B\Omega^2)\cos\Omega T - (2\dot{B}\Omega + C\Omega^2)\sin\Omega T. \tag{17}$$

We consider trajectories close to periodic solutions, so that the amplitude functions vary slowly with time. This enables us to neglect the second order derivatives. This has been done somewhat in the spirit of first-order averaging [39,40]. Substituting Eqs. (15)–(17) in Eq. (6), and balancing the coefficients of the constant terms and $\sin\Omega T$ and $\cos\Omega T$ we obtain

$$2A^3 - 6A^2 + (3R^2 + 4)A + 2\lambda Q - 3R^2 = 0, \tag{18}$$

$$-8\frac{\Omega}{D_e^2}\dot{B} + 8C - 4\frac{\Omega^2}{D_e^2}C + 3R^2C - 24AC + 12A^2C + 4\lambda N = 0, \tag{19}$$

and

$$8\frac{\Omega}{D_e^2}\dot{C} + 8B - 4\frac{\Omega^2}{D_e^2}B + 3R^2B - 24AB + 12A^2B + 4\lambda M = 4F_0. \tag{20}$$

Here $R^2 = B^2 + C^2$ is the amplitude of oscillation corresponding to the excitation frequency. Similarly substituting in Eq. (7) and balancing the corresponding terms gives

$$\frac{1}{1-\beta}\dot{A} + A = Q + \dot{Q}, \tag{21}$$

$$\frac{1}{1-\beta}\Omega B - C + \dot{N} - \Omega M + N - \frac{1}{1-\beta}\dot{C} = 0, \tag{22}$$

and

$$M - B - \frac{1}{1-\beta}\Omega C + \Omega N + \dot{M} - \frac{1}{1-\beta}\dot{B} = 0. \tag{23}$$

At steady state, all time derivatives become zero, so that we can re-write our equations as

$$2A^3 - 6A^2 + (3R^2 + 4)A + 2\lambda Q - 3R^2 = 0, \tag{24}$$

$$8D_e^2C - 4\Omega^2C + 3D_e^2R^2C - 24D_e^2AC + 12D_e^2A^2C + 4D_e^2\lambda N = 0, \tag{25}$$

$$8D_e^2B - 4\Omega^2B + 3D_e^2R^2B - 24D_e^2AB + 12D_e^2A^2B + 4D_e^2\lambda M = 4D_e^2F_0, \tag{26}$$

$$A = Q, \tag{27}$$

$$\frac{1}{1-\beta}\Omega B - C - \Omega M + N = 0, \tag{28}$$

and

$$M - B - \frac{1}{1-\beta}\Omega C + \Omega N = 0. \tag{29}$$

It can be seen that if $R = 0$, from Eqs. (24) and (27), we obtain the equilibrium points for the unforced system as

$$A = 0 \qquad \text{and} \qquad A = \frac{3}{2} \pm \frac{\sqrt{1-4\lambda}}{2}. \tag{30}$$

Since Eqs. (28) and (29) are linear equations, we can directly solve them for the coefficients M and N. Thus we have

$$M = \frac{B\Omega^2 + \Omega\beta C - B\beta + B}{(1-\beta)(1+\Omega^2)}, \tag{31}$$

and

$$N = \frac{C\Omega^2 - \Omega\beta B + C - \beta C}{(1-\beta)(1+\Omega^2)}. \tag{32}$$

Substituting Eqs. (31) and (32) in Eqs. (25) and (26) we get equations of the form

$$\zeta B + \xi C = 0, \tag{33}$$

and

$$\xi B - \zeta C = 4D_e^2F_0, \tag{34}$$

where

$$\zeta = -\frac{4D_e^2\lambda\Omega\beta}{(1-\beta)(1+\Omega^2)} \qquad \text{and}$$

$$\xi = 12D_e^2A^2 + 3D_e^2R^2 - 24D_e^2A + \frac{4D_e^2\lambda(\beta - 1 - \Omega^2)}{(\beta-1)(1+\Omega^2)} + 8D_e^2 - 4\Omega^2. \tag{35}$$

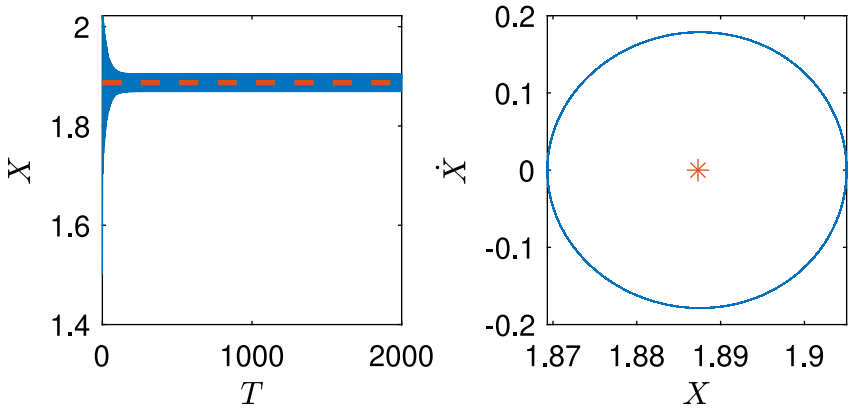

(a) $F_0 = 0.01$

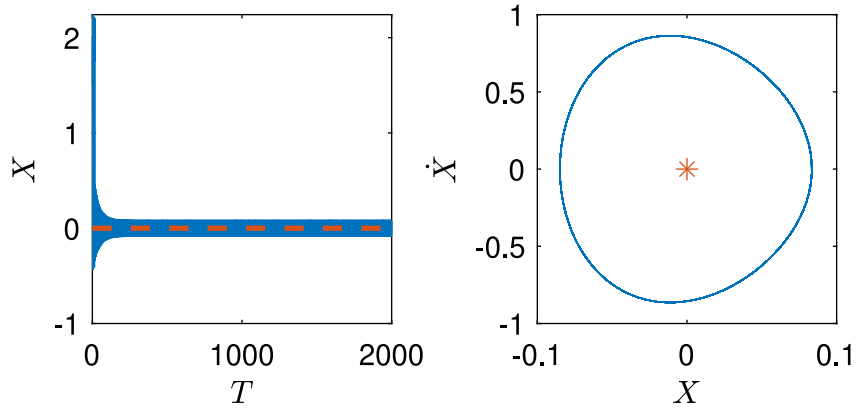

(b) $F_0 = 0.1$

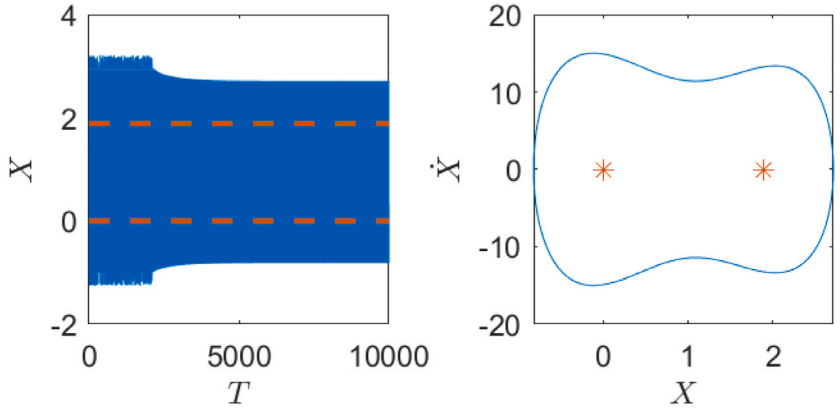

(c) $F_0 = 0.5$

Fig. 3. Time domain simulations for $\Omega = 10$, $D_e = 10$, $\beta = 0.5$, $\lambda = 0.1$ (a) small amplitude intrawell motion; the motion stays confined to the potential well it started from. (b) Permanent escape from potential well; after some initial cross-well transients, the motion settles in a different potential well than the one it started from. (c) Well hopping motion; the system transitions between the two potential wells. The red dashed line and the red stars indicate the equilibrium positions.

Squaring and adding Eqs. (33) and (34), we get

$$R^2(\zeta^2 + \xi^2) = 16 D_e^4 F_0^2. \tag{36}$$

Eq. (24) together with Eq. (36) are used to find the mean (A) and amplitude (R) of the steady-state solutions (note that Q has been eliminated from Eq. (24)). Solving this system of equations leads to multiple coexisting solutions for some parameter values. Hence, the question of their stability naturally arises. To determine the stability of the solutions, the equations are cast in the form of

$$\dot{U} = f(U), \tag{37}$$

where $U = [A, B, C, M, N]^T$. The eigenvalues of the Jacobian of $f(U)$ evaluated at the steady-state solutions determine the stability of the solutions. If the real part of all the eigenvalues is negative, then the solution is stable. If at least one of the eigenvalues has a positive real part, then the solution is unstable.

The amplitude of steady-state solutions (R) for a forcing amplitude of $F_0 = 1$ is shown in Fig. 4(a). The stable solutions are indicated by the solid blue lines while the unstable solutions are indicated by the red dashed lines. It can be seen that in the low frequency regime, the large-amplitude cross-well motion is the only stable periodic solution. As the frequency increases, this periodic orbit becomes unstable through

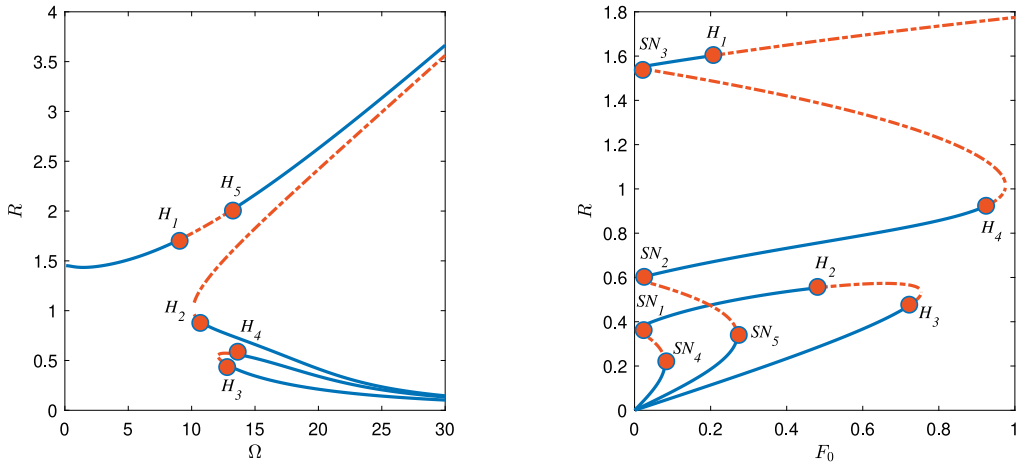

(a) Frequency response for $F_0 = 1$

(b) Amplitude Response for $\Omega = 10$

Fig. 4. Amplitude of steady state solutions for the first order truncated Fourier series. Solid blue lines indicate stable solutions. Red dashed lines indicate unstable solutions. Saddle node bifurcation points are indicated by SN and Hopf bifurcation points are indicated by H. The subscript represents the order in which they occur as the forcing parameter is increased. System parameter values are $D_e = 10, \beta = 0.5, \lambda = 0.1$. (For interpretation of the references to color in this figure legend, the reader is referred to the web version of this article.)

a Hopf bifurcation (H_1) and once again stabilizes through a Hopf bifurcation (H_5). An unstable branch of solution arises around $\Omega \approx 12.1$, which forms a loop that stabilizes through two Hopf bifurcations H_3 and H_4. This branch corresponds to oscillations about the inverted configuration.

The response curve corresponding to the forcing amplitude is shown in Fig. 4(b). It can be seen that there are multiple coexisting stable solutions, and the initial conditions determine which periodic attractor the system gets attracted to. For low forcing amplitudes and small initial indentations, intrawell oscillations are the only stable motion for a wide range of initial conditions. For large initial conditions, one can expect to reach the upper stable branch of solutions in the low forcing amplitude range. The saddle node and Hopf bifurcations are marked in the figure.

4.2. 2-term approximation

As stated earlier, a bistable system such as ours, coupled to a viscoelastic equation, may diffuse energy into the fractional and integer order harmonics of the forcing frequency due to the presence of quadratic and cubic nonlinearities, especially in the presence of hard forcing. Hence, it is highly likely that the dynamics will be a collective contribution of several harmonics. Numerical simulations reveal that, in the low frequency range, the response will have a dominant component at the excitation frequency and three times the excitation frequency.

With this motivation, we now extend the previous one-term approximation to a two-term approximation by considering the third-order superharmonic response.

Thus we have,

$$X(T) = A(T) + B_1(T)\cos\Omega T + C_1(T)\sin\Omega T + B_3(T)\cos 3\Omega T + C_3(T)\sin 3\Omega T, \tag{38}$$

and

$$\Sigma(T) = Q(T) + M_1(T)\cos\Omega T + N_1(T)\sin\Omega T + M_3(T)\cos 3\Omega T + N_3(T)\sin 3\Omega T. \tag{39}$$

In addition, we introduce two amplitudes, $R_1 = \sqrt{B_1^2 + C_1^2}$ and $R_3 = \sqrt{B_3^2 + C_3^2}$ corresponding to the respective frequency of oscillation. Following a similar procedure as outlined in the previous section, we obtain the amplitude and frequency response as shown in Fig. 5.

The response (R_1) corresponding to the excitation frequency is shown in Fig. 5(a) and the corresponding mean of the oscillations is shown in Fig. 5(b). It can be seen that around $\Omega = \Omega_n/3$ (here Ω_n is the linearized natural frequency about the naturally stable equilibrium; for more details on the calculation of the natural frequency, one may refer to Appendix.), the two-term Fourier series predicts an unstable branch of solutions that were not obtained from the single-term approximation, which is shown as the blue region in Figs. 5(a) and 5(b). Thus, the single-term approximation is unable to capture the full dynamics of the system. Nevertheless, the 2 term approximation still predicts the large-amplitude motions that are stable in the low frequency range although they lose their stability through a Hopf bifurcation at a much lower frequency. It can be seen that these kinds of bistable systems offer a distinct advantage in terms of having a large amplitude periodic attractor over a broad range of frequencies, which in this case is shown for $\Omega < 4$ and over $\Omega = 12.1$ to $\Omega = 30$. Although these large-amplitude solutions may coexist with other intra-well solutions, there is a range of frequencies where the large-amplitude solution is the only stable solution and hence guarantees vigorous motion. In parameter regimes where interwell solutions coexist with intrawell solutions, the primary design hurdle lies in extracting the large-amplitude motion, given the sensitivity to initial conditions and the complexities of basin of attractions, some of which may not be readily accessible or could involve interwell chaotic oscillations. The sensitivity of the system to initial conditions in the multi-solution regime has been shown in Fig. 7. It can be seen that even for a very small change in the initial condition, the system might jump from a low orbit attractor to a high orbit attractor.

The amplitude response (response of the system to the forcing amplitude F_0) is shown in Fig. 6(a) and the corresponding mean of the response in Fig. 6(b). The overall configuration of the amplitude response diagram remains the same as the single-term approximation, except for a slight shift in the upper branch of the solution. Once again we see that the intra-well and the inter-well oscillations coexist with each other. To determine the nature of the Hopf bifurcations, one has to go beoynd the linear stability analysis and rely on softwares like MATCONT. For example, it can be seen that beyond the Hopf bifurcation H_4, there are no stable perioidic orbits. Numerical continuation in MATCONT suggests that there are stable limit cycles to the left of H_4, but none just to its right. This indicates that the Hopf bifurcation is a subcritical one, which is further confirmed by the postive first Lyapunov coefficient. Beyond H_4, the system simply gets attracted to

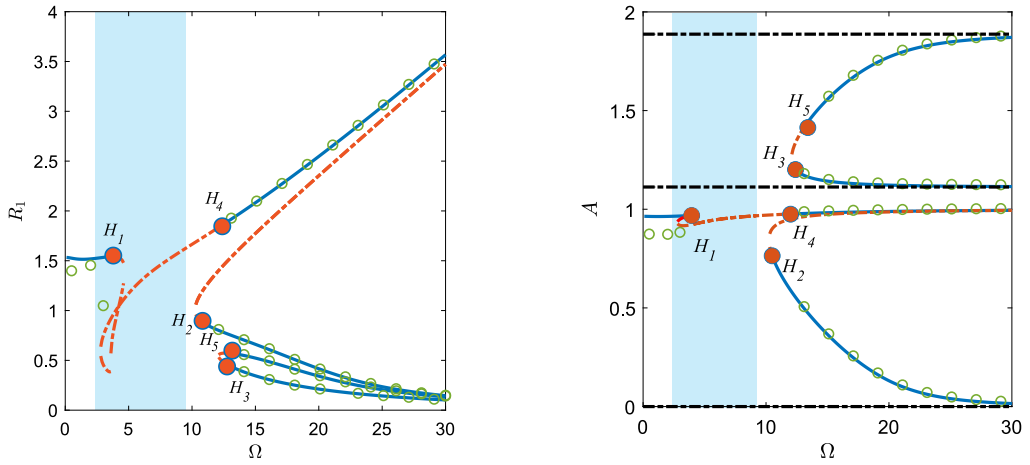

(a) Amplitude of response for $F_0 = 1$ (b) Mean of response for $F_0 = 1$

Fig. 5. Amplitude and mean of steady state solutions for the second order truncated Fourier series. Solid blue lines indicate stable solutions. Red dashed lines indicate unstable solutions. Black dashed lines indicate the equilibrium positions of the system. Green circles denote amplitudes and means obtained from time-domain simulations. The Hopf bifurcation points are indicated by H. The subscript represents the order in which they occur as the forcing parameter is increased. System parameter values are $D_e = 10, \beta = 0.5, \lambda = 0.1$. (For interpretation of the references to color in this figure legend, the reader is referred to the web version of this article.)

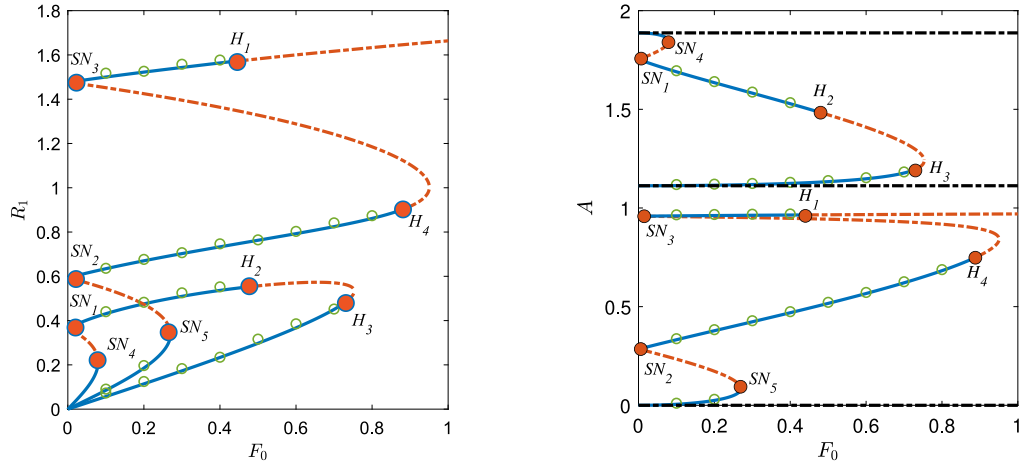

(a) Amplitude of response for Ω = 10 (b) Mean of response for Ω = 10

Fig. 6. Amplitude and mean of steady state solutions for the second order truncated Fourier series. Solid blue lines indicate stable solutions. Red dashed lines indicate unstable solutions. Black dashed lines indicate the equilibrium positions of the system. Green circles denote amplitude and means obtained from time-domain simulations. The saddle node bifurcation points are indicated by SN and the Hopf bifurcation points are indicated by H. The subscript represents the order in which they occur as the forcing parameter is increased. System parameter values are $D_e = 10, \beta = 0.5, \lambda = 0.1$. (For interpretation of the references to color in this figure legend, the reader is referred to the web version of this article.)

the nearest attractor, which may be a periodic attractor (that is not captured by the two-term approximation) or a chaotic attractor.

The frequency and amplitude responses have also been verified using numerical simulations as shown by the green circles in Figs. 5 and 6 . The numerical simulations reveal that for regions where multiple stable solutions exist, the system is highly sensitive to the initial conditions (see Fig. 7), which dictate which basin of attraction the system is attracted to. Also some of the basins of attraction are not easily accessible, hence a very small change in initial conditions is needed to get on the steady-state curves. It can also be seen that in the low frequency range, the match between the numerical and analytical results are not that great. This is because of the interaction between the slow and fast time scales in this parameter regime that leads to several sub- and superharmonic frequencies getting excited. Thus, a higher-order truncation of the Fourier series is needed to accurately capture the dynamics in this range.

The variation of the frequency response curves with the geometric parameter λ for different Deborah numbers is shown in Fig. 8. Four ranges of Deborah numbers have been considered, namely (i) $D_e \gg 1$, (ii) $D_e > 1$, (iii) $D_e = 1$, and (iv) $D_e \ll 1$. λ also denotes the strength of the coupling between the elastic von Mises truss and the viscoelastic element. As λ increases, the linear stiffness of the system grows, and hence the system shows hardening behavior. Thus, the natural frequency of the system increases (see Appendix). As the geometric parameter increases beyond the transition point from bistable to monostable behavior, the lower branch of solutions corresponding to oscillations about the inverted configuration vanishes. We observe the same behavior across different ranges of Deborah numbers. However, the behavior near one-third of the natural frequency is different in each case. We observe that for high Deborah numbers ($D_e = 100$), the curve bends toward the right, thus indicating a hardening behavior in this range, before turning back on itself. For lower D_e's, the bend to the right is not observed, although the curve still loops back on itself before merging with the stable large-amplitude branch.

The variation in frequency response with the relaxation parameter β for different Deborah numbers is shown in Fig. 9. It can be seen that for

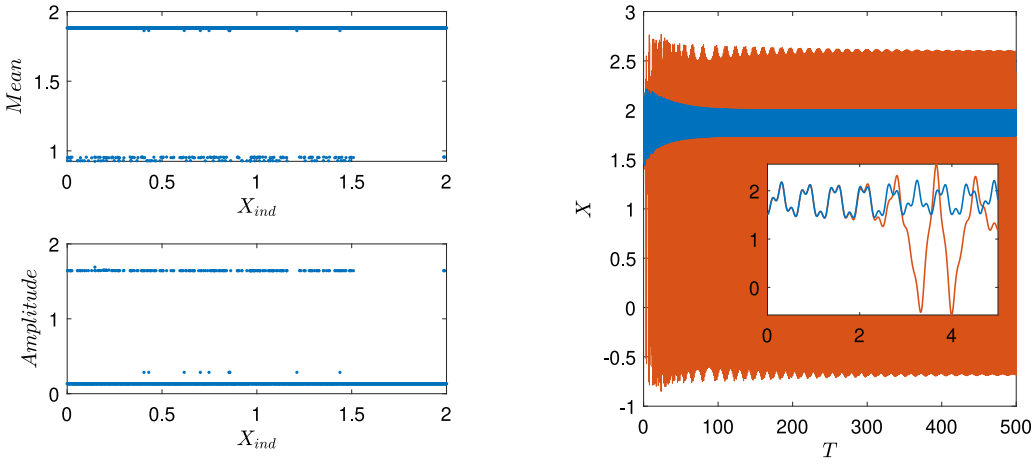

(a) Mean and amplitude of response against indentation depth for $\Omega = 30$ (b) Time response for $X_{ind} = 1.51$ (blue curve) and $X_{ind} = 1.509$ (red curve)

Fig. 7. Variation of the mean and amplitude of the steady state solutions with the indentation depth. The system is sensitive to the initial conditions where there are multiple coexisting solutions. System parameter values are $D_e = 10, \beta = 0.5, \lambda = 0.1, F_0 = 1$.

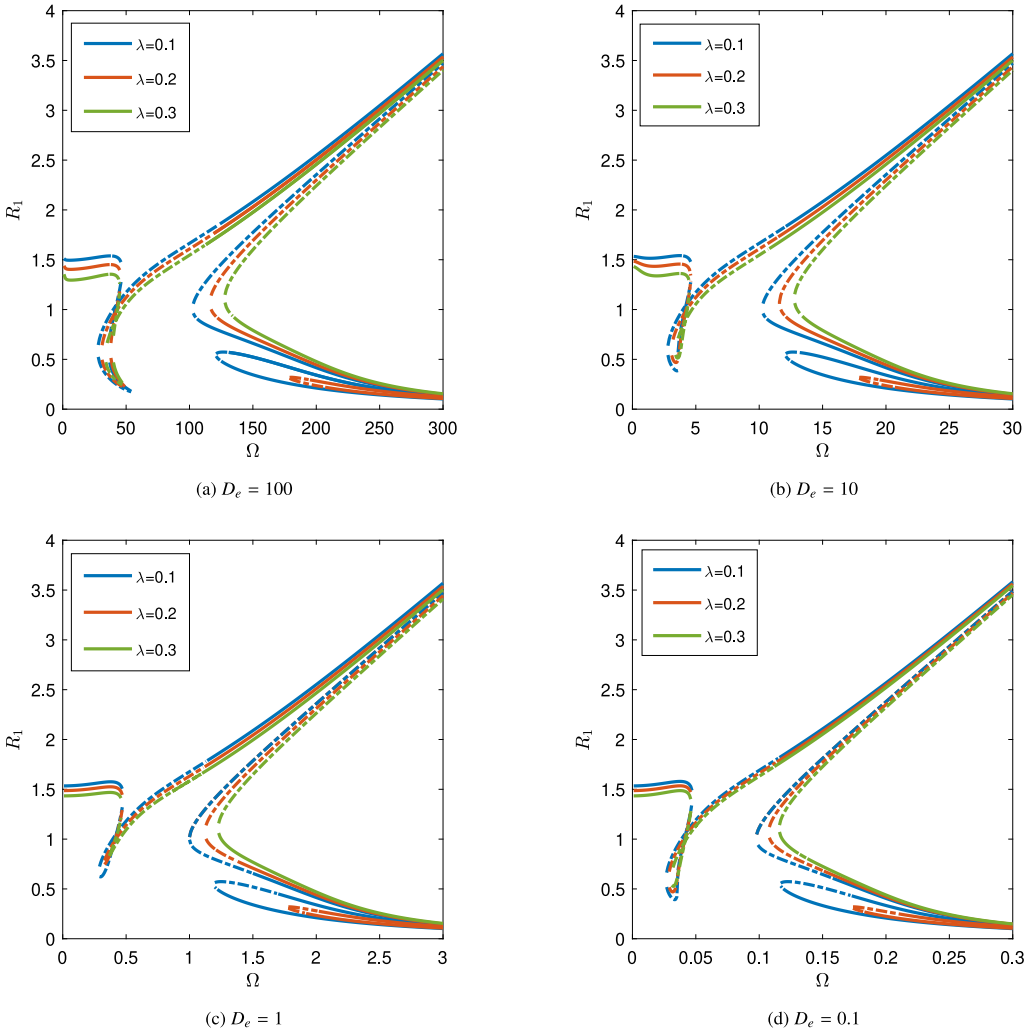

(a) $D_e = 100$ (b) $D_e = 10$

(c) $D_e = 1$ (d) $D_e = 0.1$

Fig. 8. Variation of frequency response with λ in different ranges of Deborah number for $F_0 = 1, \beta = 0.5$. Solid lines indicate stable solutions. Dashed lines indicate unstable solutions. (For interpretation of the references to color in this figure legend, the reader is referred to the web version of this article.)

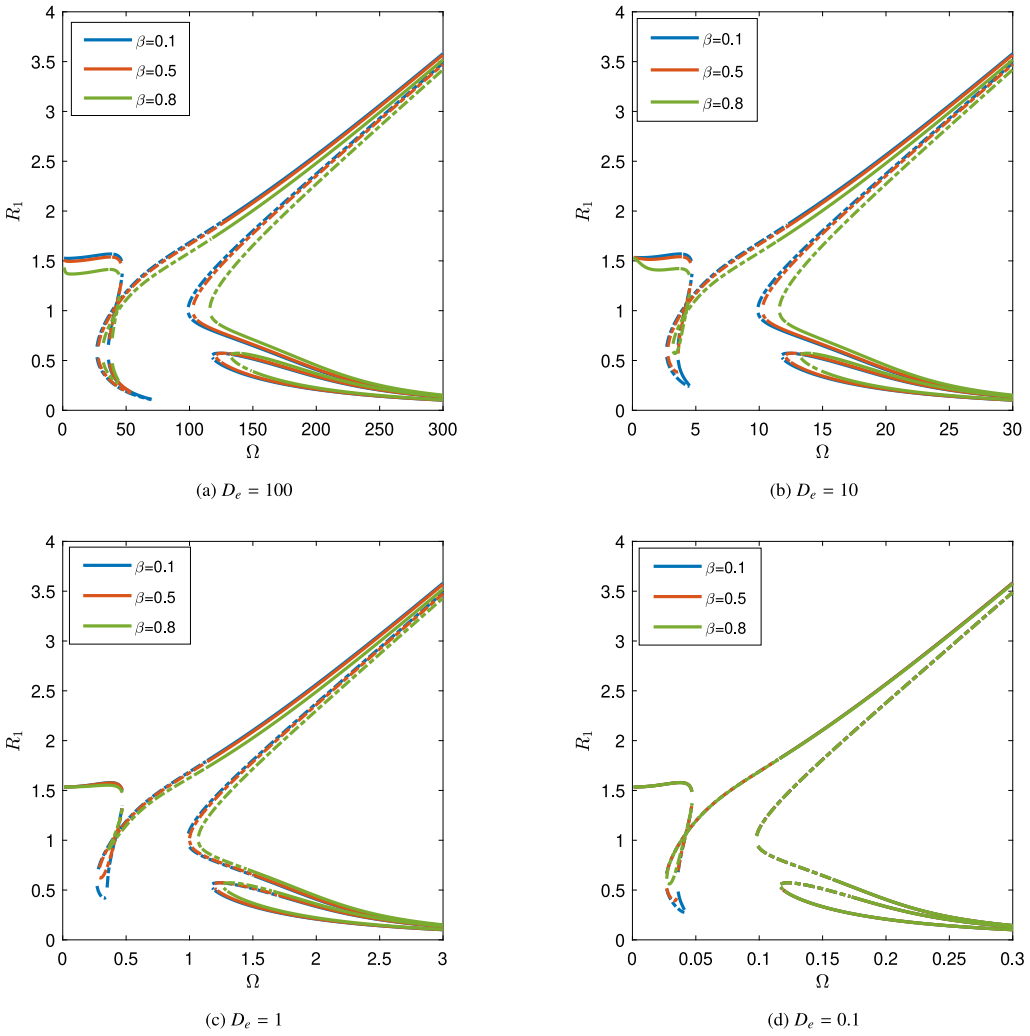

(a) $D_e = 100$ (b) $D_e = 10$

(c) $D_e = 1$ (d) $D_e = 0.1$

Fig. 9. Variation of frequency response with β in different ranges of Deborah number for $F_0 = 1, \lambda = 0.1$. Solid lines indicate stable solutions. Dashed lines indicate unstable solutions. (For interpretation of the references to color in this figure legend, the reader is referred to the web version of this article.)

lower ranges of D_e, the effect of β on the frequency response, especially in the high frequency range, is not significant. As D_e increases, the effect on frequency response becomes more prominent. For higher Deborah numbers, it is apparent that when β is small ($\beta \lesssim 0.5$), there is minimal change in the frequency response with respect to β. This phenomenon arises due to the hyperbolic dependence ($\sim \frac{\beta}{1-\beta}$) of the response on β, which results in notable distinctions primarily when $\beta \to 1$. As β increases, the frequency response shifts towards higher frequencies, indicating a trend towards hardening behavior.

The interest in these types of bistable systems is due to their applications in vibration attenuation [41,42]. Hence, it is worthwhile to study the energy dissipated by the system when subjected to external harmonic excitation. The average energy dissipated at steady state over a period of $T = 2\pi/\Omega$ can be calculated as

$$E_{st} = \frac{1}{T}\int_0^{T=2\pi/\Omega} \Sigma \dot{X} dT, \tag{40}$$

or

$$E_{st} = \frac{\Omega^2\beta}{2(1+\Omega^2)(1-\beta)} R_1^2 + \frac{9\Omega^2\beta}{2(1-\beta)(1+9\Omega^2)} R_3^2. \tag{41}$$

Note that M_1, N_1, M_3, N_3 have been eliminated from the linear steady state equations. The average energy dissipated per cycle is shown in Fig. 10 and has also been verified numerically as shown by the green circles. It can be seen from Eq. (41), that with increase in β the quantity $\frac{\beta}{1-\beta}$ increases monotonically. However, it must be noted that β also determines the amount of damping in the system. An increase in β increases the amount of damping and hence restricts the amplitude of oscillations R_1 and R_3. Thus there exists an optimum value of β that allows for maximum energy dissipation.

The average energy dissipated per cycle is shown in Fig. 11(a) as a function of β for $F_0 = 1, \Omega = 10$. It can be seen that in the purely elastic limit at $\beta = 0$, there is no energy dissipation. As β increases, the dissipation energy also increases. There exists a particular value of β (β_{opt}) at which the dissipated energy reaches its peak ($E_{st_{max}}$) for a given set of excitation parameters. Beyond this value, the dissipated energy starts decreasing because in this regime, the amplitude of oscillations are highly restricted by the damping in the system. The variation of the optimum value of β against the forcing parameters is shown in Fig. 11(b). It can be seen that β_{opt} increases monotonically with F_0 and subsequently settles to a constant value. For very low values of Ω ($\leqq 3$), β_{opt} decreases until it reaches a minimum, beyond which it increases monotonically (this variation is, however, in a very narrow range, in the high β regime). Hence, the analytical approach to the problem through the harmonic balance method allows us to design an optimum system for maximum vibrational energy dissipation for a given set of operating parameters.

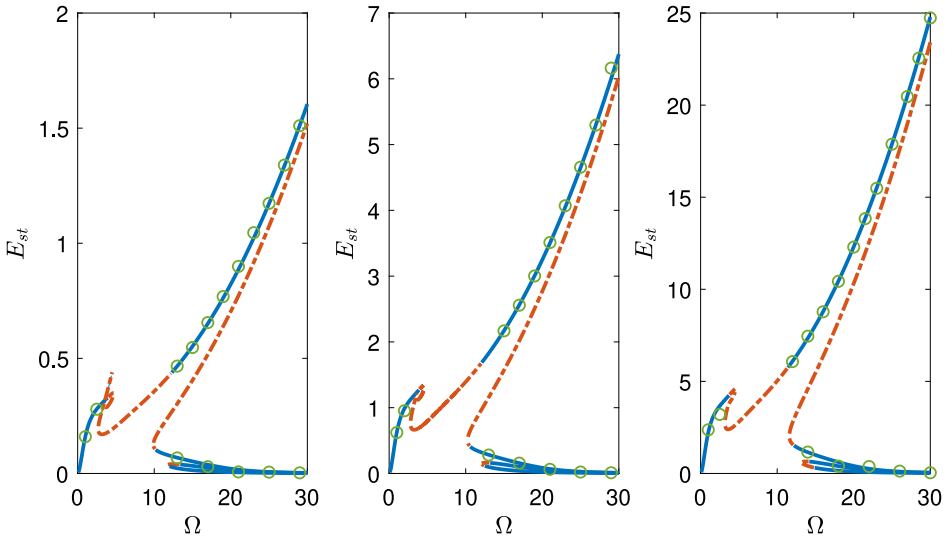

Fig. 10. Average energy dissipated in a cycle for $\lambda = 0.1, D_e = 10, F_0 = 1$ and $\beta = [0.2, 0.5, 0.8]$. Solid blue lines correspond to stable solutions. Red dashed lines correspond to unstable solutions. Green circles denote average energy dissipated obtained from numerical simulations. (For interpretation of the references to color in this figure legend, the reader is referred to the web version of this article.)

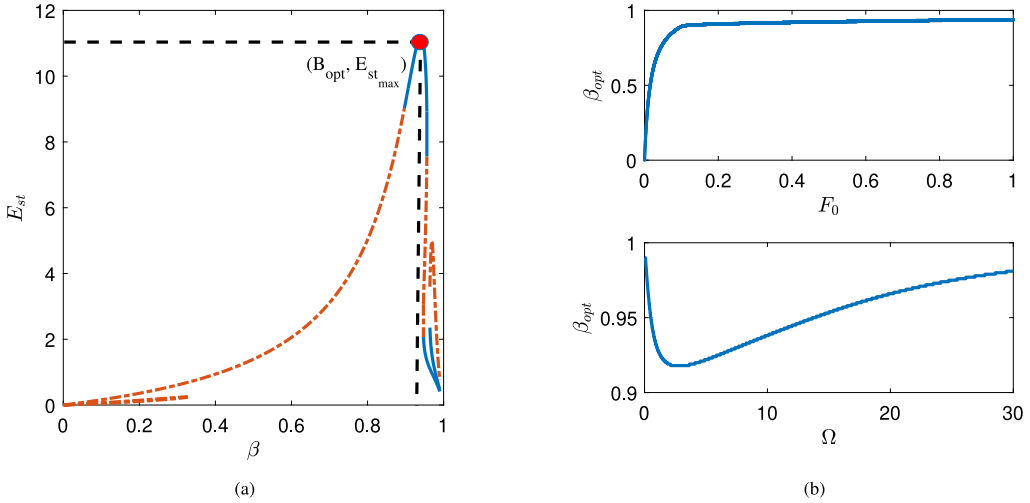

Fig. 11. (a) Average energy dissipated per cycle as a function of β for $D_e = 10, \lambda = 0.1, F_0 = 1, \Omega = 10$. Solid blue lines correspond to stable solutions. Red dashed lines correspond to unstable solutions. (b) Variation of the optimum value of β with the forcing amplitude and the forcing frequency as obtained from the single-term harmonic balance. (For interpretation of the references to color in this figure legend, the reader is referred to the web version of this article.)

5. Equivalent viscous systems

Now that we have an understanding of the viscoelastic system, we perform a thought experiment. Is it possible to formulate an equivalent viscous system that can faithfully reproduce the dynamics of the viscoelastic system without introducing any additional complexities in the equations? In other words, we aim to show the need to include viscoelasticity in the model, without which some important features in the dynamics may not be captured accurately. Note that eliminating viscoelasticity will not lead to analytical results or reduce computational times. It simply enables us to do a lower-order parametric study to understand the behavior of the system. The key consideration here is whether such a basic simplification suffices to adequately capture the dynamics of the system. With this motivation, we follow an energy-based approach to derive an equivalent linear damped system (see Fig. 12).

We start with the dimensional form of the equation for the viscoelastic element in Eq. (3). Taking a Laplace transform of the equation, we have

$$\frac{k_1 + k_2}{k_2}[s\bar{X} - x(0)] + \frac{k_1}{c}\bar{X} = \frac{1}{k_2}[s\bar{F}_v - f_v(0)] + \frac{1}{c}\bar{F}_v, \tag{42}$$

where $\bar{X}$ and $\bar{F}_v$ are the Laplace transform of x and f_v. Assuming that at $t = 0$, the initial displacement and the viscoelastic reaction force are zero, we have

$$\bar{F}_v = \left[\frac{(k_1 + k_2)sc + k_1k_2}{k_2 + sc}\right]\bar{X}. \tag{43}$$

Now, assuming that the mass exhibits a sinusoidal displacement of $x = X_0 \sin \omega t$ (in line with the assumption that the initial displacement is zero), we have

$$\bar{F}_v = \left[\frac{(k_1 + k_2)sc + k_1k_2}{k_2 + sc}\right]\frac{X_0\omega}{\omega^2 + s^2}. \tag{44}$$

Now, taking the inverse Laplace transform, we obtain

$$f_v = X_0k_1 \sin \omega t + \frac{X_0\omega^2c^2k_2}{\omega^2c^2 + k_2^2}\sin \omega t + \frac{X_0\omega ck_2^2}{\omega^2c^2 + k_2^2}\cos \omega t - \frac{X_0\omega ck_2^2}{\omega^2c^2 + k_2^2}e^{-\frac{k_2 t}{c}}.$$

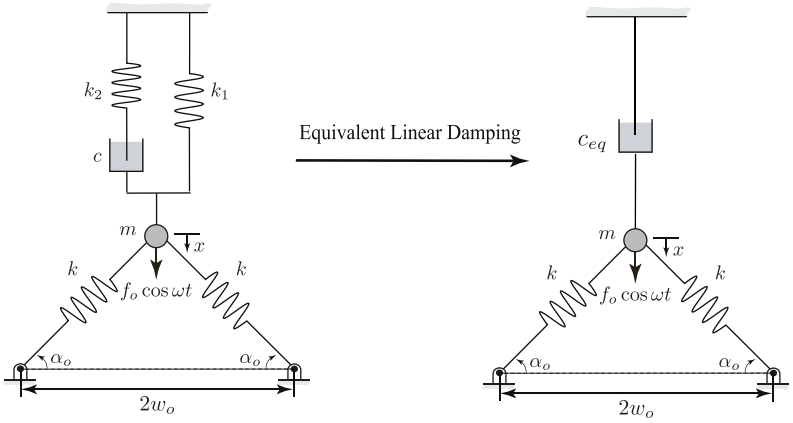

Fig. 12. Equivalent viscous model obtained from the viscoelastic system by an energy based approach.

(45)

Note that the last term in the above expression goes to zero, as $t \to \infty$. Thus, at steady state, the reactive viscoelastic force will be harmonic as well (although out of phase).

The energy dissipated by the viscous damper in the standard linear solid element in a single cycle at steady state (by neglecting the exponentially decaying term) can be found as

$$U_d = \int_0^{2\pi/\omega} f_v \dot{x} dt = \frac{X_0^2 \pi c k_2^2 \omega}{\omega^2 c^2 + k_2^2}. \tag{46}$$

The energy dissipated in a single cycle as a result of viscous damping alone in the presence of a harmonic excitation is given by

$$U_d = \pi c_{eq} X_0^2 \omega. \tag{47}$$

Thus, equivalent viscous damping can be found by equating the energies dissipated in a single cycle by the viscous and the viscoelastic system as

$$c_{eq} = \frac{k_2^2 c}{k_2^2 + \omega^2 c^2}. \tag{48}$$

Note that the equivalent damping coefficient depends on the frequency of oscillation. Hence, the modified equations of motion are now given by

$$m\ddot{x} - \frac{kx}{w_0^2}(x - 2\alpha_0 w_0)(\alpha_0 w_0 - x) + \frac{k_2^2 c}{\omega^2 c^2 + k_2^2}\dot{x} = f \cos \omega t. \tag{49}$$

Eq. (49) is now non-dimensionalized using the same scheme that was used for the viscoelastic system. Thus, we have

$$\frac{1}{D_e^2}\frac{d^2X}{dT^2} - 3X^2 + X^3 + 2X + \frac{\beta\lambda}{(1-\beta)(1+\Omega^2)}\frac{dX}{dT} = F_0 \cos \Omega T. \tag{50}$$

It can be seen that for low oscillation frequencies, the frequency dependence of the damping no longer exists, and it is possible to obtain an constant equivalent damping coefficient. Conversely, for high excitation frequencies, the frequency dependence of the damping becomes significant and cannot be neglected. It is crucial to recognize that though the equivalent viscous system might seem straightforward, it carries potential pitfalls. We note that the validity of this approach is based on the premise that the response itself is harmonic. Hence, this method is unable to replicate the quasiperiodic or chaotic motions of the system exactly. This is evident from Fig. 13(a) in which a large-amplitude harmonic response of the original system matches perfectly with that of the equivalent system. If the response is not harmonic as in Fig. 13(b), the equivalent system may or may not track the original response depending on the forcing and system parameters. Although the two curves in Fig. 13(b) are slightly out of phase (as was alluded to in the derivation), the amplitudes are still slightly off but give a reasonable match. Hence, an important criterion for this method to yield reliable approximations is that of the harmonic response.

Fig. 14 shows the steady-state root mean square errors between the time response of the viscoelastic system and the equivalent system. The validity of the approximate model depends both on the forcing parameters as well as the intrinsic system parameters. It can be seen that in the low D_e range, the match between the two systems is almost exact for both the resonant and non-resonant frequencies. As D_e increases, a band of large errors (as shown by the red dashed lines) is obtained for all ranges of β. Beyond this band, the error in the high β range is significantly lower compared to the low β range for the range of D_e considered. Thus, while the approximate viscous model might have high fidelity in some parameter regimes, its accuracy decreases in other parameter regimes. The response characteristics of the system and the system parameters in the operating range may not be known a priori. Hence, relying solely on a simplistic viscous model may produce misleading results, thus emphasizing the need for a full-scale viscoelastic model.

6. Discussion and conclusion

In this paper, we studied the effects of viscoelasticity on the periodic response of a harmonically forced bistable von Mises truss. Despite its apparent simplicity, the viscoelastic von Mises truss allows us to address critical questions in nonlinear dynamics, capturing the interplay between geometric and material parameters within the system. Moreover, it represents a broad class of dynamical systems, including shells and arches, and facilitates lumped parameter analysis when a continuum approach becomes tedious.

We showed that viscoelasticity introduces an additional degree of freedom into the system, resulting in even more complex dynamics than is typical in the viscous counterpart. While the chaotic motion of this system has been extensively studied, our work diverges by concentrating on regular solutions, specifically large amplitude periodic solutions, for which there is limited analytical treatment in existing literature. Understanding these periodic motions is crucial due to their applications in energy harvesting and vibration suppression. For systems with multiple potential wells, several co-existing periodic solutions can arise, necessitating a systematic study of the system. These coexisting solutions make the system sensitive to initial conditions that determine which basin of attraction the system gravitates towards. Some basins of attraction are more accessible than others, making it essential to quantify the parameter regimes where this behavior is likely. In this paper, we use the harmonic balance method to predict the onset of large amplitude motions and the transition from intrawell to crosswell motion. The effects of parameter variation have been shown for different parameter regimes through bifurcation diagrams. The harmonic

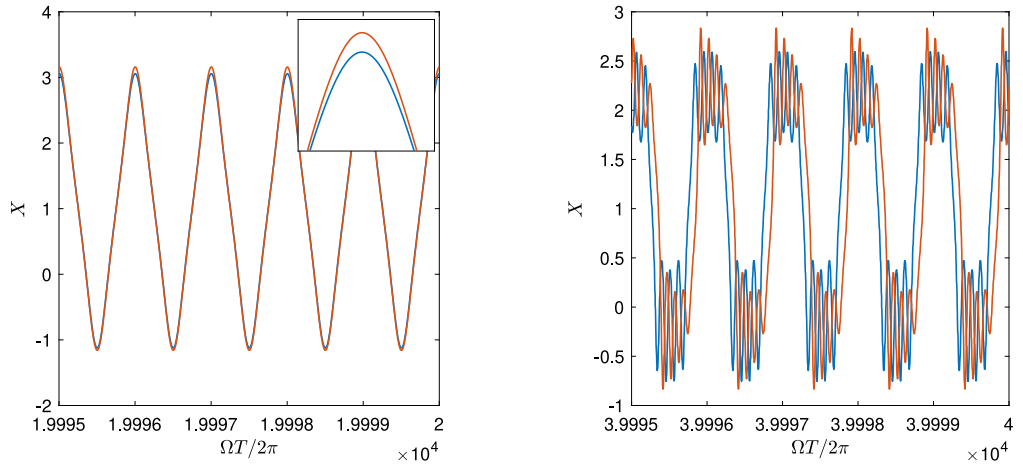

(a) Minute deviation in tracking of original response

(b) Reasonable tracking of original response

Fig. 13. Comparison of steady state time responses of viscoelastic system and equivalent viscous system for (a) $F_0 = 1, \Omega = 13, D_e = 10, \beta = 0.5, \lambda = 0.1$ (b) $F_0 = 1, \Omega = 2, D_e = 10, \beta = 0.5, \lambda = 0.1$. The blue line corresponds to the viscoelastic system, and the red line corresponds to the viscous system. (For interpretation of the references to color in this figure legend, the reader is referred to the web version of this article.)

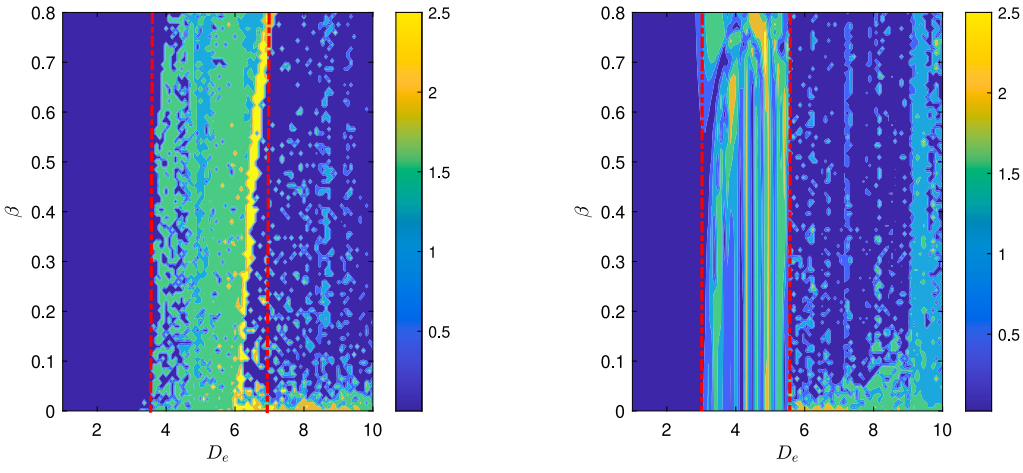

(a) Ω = 14

(b) Ω = 10

Fig. 14. Steady state root mean square errors between time domain simulations of viscoelastic system and equivalent viscous system for (a) $F_0 = 1, \Omega = 14$ (at resonant frequency), $D_e = 10, \beta = 0.5, \lambda = 0.1$ (b) $F_0 = 1, \Omega = 10$ (away from resonant frequency), $D_e = 10, \beta = 0.5, \lambda = 0.1$. The first 50000 periods have been removed to eliminate transients. Cooler colors represent lower error, while hotter colors represent higher errors. The red dashed lines show the Deborah number band with high error. (For interpretation of the references to color in this figure legend, the reader is referred to the web version of this article.)

balance method allowed us to find optimum system parameters for maximum energy dissipation for a given operating condition.

Finally, we formulated an equivalent viscous system using an energy-based approach. We demonstrated that a naive viscous approximation has potential pitfalls in the high-frequency regime as well as for some combination of system parameters, thus having high fidelity in some parameter regimes and low fidelity in others. Hence, to faithfully recreate the dynamics of the system, analysis of the full-scale viscoelastic system is essential.

This work lays a significant foundation for future research. The harmonic balance method shows that the system can exhibit two types of motion: small amplitude oscillations about the stable equilibria and large amplitude oscillations about the unstable equilibrium. Regardless of the system or excitation parameters, it is impossible to extract small amplitude oscillations about the saddle node under external harmonic excitation. However, alternative forms of excitation might enable the extraction of such oscillations for specific parameter combinations. This capability allows for temporarily parking the system in the unstable state and subsequently biasing it towards one of the stable states depending on the external perturbation. This concept has wide applications in mechanical logic gates, mechanically actuated sensors, and programmable metamaterials.

CRediT authorship contribution statement

Pritam Ghoshal: Writing – original draft, Methodology, Formal analysis. **James M. Gibert:** Writing – review & editing, Project administration, Methodology, Funding acquisition, Conceptualization. **Anil K. Bajaj:** Writing – review & editing, Project administration, Methodology.

Declaration of competing interest

The authors declare that they have no known competing financial interests or personal relationships that could have appeared to influence the work reported in this paper.

Data availability

Data will be made available on request.

Acknowledgments

The authors would like to acknowledge the financial support provided by NSF CAREER Award: CMMI 2145803. During the preparation of this work the author(s) used AI tools in Overleaf in order to remove grammatical errors. After using this tool/service, the author(s) reviewed and edited the content as needed and take(s) full responsibility for the content of the publication.

Appendix. Linearized equations and natural frequencies

To find the linearized equations and the corresponding natural frequencies, we first write the governing equations of the unforced system as a set of first order differential equations. Thus we have

$$\begin{aligned} \dot{x_1} &= x_2, \\ \dot{x_2} &= D_e^2 x_1(x_1-2)(1-x_1) - \lambda D_e^2 x_3, \\ \dot{x_3} &= \frac{1}{1-\beta} x_2 + x_1 - x_3. \end{aligned} \tag{A.1}$$

For oscillations about the natural configuration, we consider $x_1 = x_2 = x_3 = 0$ and impose a small perturbation to the system. Thus we have $x_1 = \xi_1$, $x_2 = \xi_2$ and $x_3 = \xi_3$, where ξ_1, ξ_2 and ξ_3 are small quantities. Substituting and linearizing the equations we have

$$\begin{bmatrix} \dot{\xi_1} \\ \dot{\xi_2} \\ \dot{\xi_3} \end{bmatrix} = \begin{bmatrix} 0 & 1 & 0 \\ -2D_e^2 & 0 & -\lambda D_e^2 \\ 1 & \frac{1}{1-\beta} & -1 \end{bmatrix} \begin{bmatrix} \xi_1 \\ \xi_2 \\ \xi_3 \end{bmatrix}. \tag{A.2}$$

The eigenvalues of this matrix gives the natural frequency. On the contrary, if the equations are linearized about the inverted configuration ($x_1 = x_3 = \frac{3}{2} + \frac{\sqrt{1-4\lambda}}{2}, x_2 = 0$), then the equations take the form

$$\begin{bmatrix} \dot{\xi_1} \\ \dot{\xi_2} \\ \dot{\xi_3} \end{bmatrix} = \begin{bmatrix} 0 & 1 & 0 \\ -\frac{D_e^2(1+3\sqrt{1-4\lambda}-6\lambda)}{2} & 0 & -\lambda D_e^2 \\ 1 & \frac{1}{1-\beta} & -1 \end{bmatrix} \begin{bmatrix} \xi_1 \\ \xi_2 \\ \xi_3 \end{bmatrix}. \tag{A.3}$$

When $\lambda = 0$, the natural frequency of oscillation about either of the two stable equilibrium positions turns out to be the same (since we have a symmetric potential well) and is equal to $\sqrt{2}D_e$. Recalling the dimensional form, this turns out to be $\sqrt{2}\alpha_0\sqrt{k/m}$. Thus, the natural frequency depends on the point mass, the stiffness of the tilted springs, and the initial inclination angle of the truss.)

References

[1] N. Hu, R. Burgueño, Buckling-induced smart applications: recent advances and trends, Smart Mater. Struct. 24 (6) (2015) 063001.
[2] Y. Cao, M. Derakhshani, Y. Fang, G. Huang, C. Cao, Bistable structures for advanced functional systems, Adv. Funct. Mater. 31 (45) (2021) 2106231.
[3] M. Gomez, D.E. Moulton, D. Vella, Dynamics of viscoelastic snap-through, J. Mech. Phys. Solids 124 (2019) 781–813.
[4] T. Liu, Y. Chen, L. Liu, Y. Liu, J. Leng, L. Jin, Effect of imperfections on pseudo-bistability of viscoelastic domes, Extreme Mech. Lett. 49 (2021) 101477.
[5] M. Gomez, D.E. Moulton, D. Vella, Critical slowing down in purely elastic 'snap-through'instabilities, Nat. Phys. 13 (2) (2017) 142–145.
[6] A. Pandey, D.E. Moulton, D. Vella, D.P. Holmes, Dynamics of snapping beams and jumping poppers, Europhys. Lett. 105 (2) (2014) 24001.
[7] M. Gomez, D.E. Moulton, D. Vella, Passive control of viscous flow via elastic snap-through, Phys. Rev. Lett. 119 (14) (2017) 144502.
[8] D.P. Holmes, A.J. Crosby, Snapping surfaces, Adv. Mater. 19 (21) (2007) 3589–3593.
[9] M. Pezzulla, N. Stoop, X. Jiang, D.P. Holmes, Curvature-driven morphing of non-Euclidean shells, Proc. R. Soc. A 473 (2201) (2017) 20170087.
[10] L. Virgin, On the elastic snapping of structural elements, Int. J. Non-Linear Mech. 149 (2023) 104329.
[11] G. Brodland, H. Cohen, Deflection and snapping of spherical caps, Int. J. Solids Struct. 23 (10) (1987) 1341–1356.
[12] H.B. Keller, E.L. Reiss, Spherical cap snapping, J. Aerosp. Sci. 26 (10) (1959) 643–652.
[13] E.L. Reiss, H.J. Greenberg, H.B. Keller, Nonlinear deflections of shallow spherical shells, J. Aeronaut. Sci. 24 (7) (1957) 533–543.
[14] L. Stein-Montalvo, P. Costa, M. Pezzulla, D.P. Holmes, Buckling of geometrically confined shells, Soft Matter 15 (6) (2019) 1215–1222.
[15] M. Taffetani, X. Jiang, D.P. Holmes, D. Vella, Static bistability of spherical caps, Proc. R. Soc. A 474 (2213) (2018) 20170910.
[16] P. Sobota, K. Seffen, Effects of boundary conditions on bistable behaviour in axisymmetrical shallow shells, Proc. R. Soc. A 473 (2203) (2017) 20170230.
[17] K.A. Seffen, S. Vidoli, Eversion of bistable shells under magnetic actuation: a model of nonlinear shapes, Smart Mater. Struct. 25 (6) (2016) 065010.
[18] A. Brinkmeyer, M. Santer, A. Pirrera, P. Weaver, Pseudo-bistable self-actuated domes for morphing applications, Int. J. Solids Struct. 49 (9) (2012) 1077–1087.
[19] P. Ghoshal, Q. Zhao, J.M. Gibert, A.K. Bajaj, Effect of boundary conditions on the stability of a viscoelastic von mises truss, in: W. Lacarbonara (Ed.), in: Advances in Nonlinear Dynamics, vol. I, Springer Nature Switzerland, Cham, 2024, pp. 217–227.
[20] E.Y. Urbach, E. Efrati, Predicting delayed instabilities in viscoelastic solids, Sci. Adv. 6 (36) (2020) eabb2948.
[21] S. Cui, R.L. Harne, Characterizing the nonlinear response of elastomeric material systems under critical point constraints, Int. J. Solids Struct. 135 (2018) 197–207.
[22] M. Amabili, Nonlinear Mechanics of Shells and Plates in Composite, Soft and Biological Materials, Cambridge University Press, 2018.
[23] P. Ghoshal, J.M. Gibert, A.K. Bajaj, The presence of chaos in a viscoelastic harmonically forced Von Mises Truss, J. Comput. Nonlinear Dyn. 19 (7) (2024).
[24] E. Loukaides, S. Smoukov, K. Seffen, Magnetic actuation and transition shapes of a bistable spherical cap, Int. J. Smart Nano Mater. 5 (4) (2014) 270–282.
[25] G. Suire, G. Cederbaum, Elastica type dynamic stability analysis of viscoelastic columns, Arch. Appl. Mech. 64 (5) (1994) 307–316.
[26] G. Suire, G. Cederbaum, Periodic and chaotic behavior of viscoelastic nonlinear (elastica) bars under harmonic excitations, Int. J. Mech. Sci. 37 (7) (1995) 753–772.
[27] S. Pourtakdoust, S. Fazelzadeh, Chaotic analysis of nonlinear viscoelastic panel flutter in supersonic flow, Nonlinear Dynam. 32 (2003) 387–404.
[28] R.S. Lakes, Viscoelastic Materials, Cambridge University Press, 2009.
[29] S. Leadenham, A. Erturk, M-shaped asymmetric nonlinear oscillator for broadband vibration energy harvesting: Harmonic balance analysis and experimental validation, J. Sound Vib. 333 (23) (2014) 6209–6223.
[30] H. Alhussein, M.F. Daqaq, Potential well escape in a galloping twin-well oscillator, Nonlinear Dynam. 99 (1) (2020) 57–72.
[31] W. Jiang, H. Shi, X. Han, L. Chen, Q. Bi, Double jump broadband energy harvesting in a Helmholtz–Duffing oscillator, J. Vib. Eng. Technol. 8 (2020) 893–908.
[32] M. Krack, J. Gross, Harmonic Balance for Nonlinear Vibration Problems, vol. 1, Springer, 2019.
[33] A.H. Alhadidi, J.M. Gibert, A new perspective on static bifurcations in the presence of viscoelasticity, Nonlinear Dynam. 103 (2) (2021) 1345–1363.
[34] R.S. Lakes, Viscoelastic Solids (1998), CRC Press, 2017.
[35] A. Brinkmeyer, A. Pirrera, M. Santer, P. Weaver, Pseudo-bistable pre-stressed morphing composite panels, Int. J. Solids Struct. 50 (7–8) (2013) 1033–1043.
[36] S.C. Stanton, B.A. Owens, B.P. Mann, Harmonic balance analysis of the bistable piezoelectric inertial generator, J. Sound Vib. 331 (15) (2012) 3617–3627.
[37] A. Arrieta, P. Hagedorn, A. Erturk, D.J. Inman, A piezoelectric bistable plate for nonlinear broadband energy harvesting, Appl. Phys. Lett. 97 (10) (2010).
[38] A. Erturk, J. Hoffmann, D.J. Inman, A piezomagnetoelastic structure for broadband vibration energy harvesting, Appl. Phys. Lett. 94 (25) (2009).
[39] A.H. Nayfeh, Perturbation Methods, John Wiley & Sons, 2008.
[40] J. Summers, M. Savage, Two timescale harmonic balance. I. Application to autonomous one-dimensional nonlinear oscillators, Phil. Trans. R. Soc. A 340 (1659) (1992) 473–501.
[41] B. Yan, N. Yu, H. Ma, C. Wu, A theory for bistable vibration isolators, Mech. Syst. Signal Process. 167 (2022) 108507.
[42] Y. Xia, M. Ruzzene, A. Erturk, Bistable attachments for wideband nonlinear vibration attenuation in a metamaterial beam, Nonlinear Dynam. 102 (2020) 1285–1296.